ADVANCED ENERGY MATERIALS
www.advenergymat.de

Rubidium Iodide Reduces Recombination Losses in Methylammonium-Free Tin-Lead Perovskite Solar Cells

Fengjiu Yang, Rowan W. MacQueen, Dorothee Menzel, Artem Musiienko, Amran Al-Ashouri, Jarla Thiesbrummel, Sahil Shah, Karunanantharajah Prashanthan, Daniel Abou-Ras, Lars Korte, Martin Stolterfoht, Dieter Neher, Igal Levine,* Henry Snaith, and Steve Albrecht**

Outstanding optoelectronic properties of mixed tin-lead perovskites are the cornerstone for the development of high-efficiency all-perovskite tandems. However, recombination losses in Sn-Pb perovskites still limit the performance of these perovskites, necessitating more fundamental research. Here, rubidium iodide is employed as an additive for methylammonium-free Sn-Pb perovskites. It is first investigated the effect of the RbI additive on the perovskite composition, crystal structure, and element distribution. Quasi-Fermi level splitting and transient photoluminescence measurements reveal that the RbI additive reduces recombination losses and increases carrier lifetime of the perovskite films. This finding is attributed to an approximately ten-fold reduction in the defect density following RbI treatment, as probed using constant final state yield photoelectron spectroscopy. Additionally, the concentration of Sn vacancies is also reduced, and the perovskite film becomes less p-type both in the bulk and at the interface towards the electron contact. Thus, the conductivity for electrons increases, improving carrier extraction. As a result, the open-circuit voltage of RbI-containing solar cells improves by 61 mV on average, with the best efficiency >20%. This comprehensive study demonstrates that RbI is effective at reducing recombination losses and carrier trapping, paving way for a new approach to Sn-Pb perovskite solar cell research.

1. Introduction

Metal halide perovskite materials have attracted worldwide attention due to their promising application as solar cell absorbers, and have undergone great strides in their development since the first report of a solar cell application appeared.[1] The tunable bandgap energy (E_g) of metal halide perovskites has led to one of the most interesting developments in this context, namely the all-perovskite tandem solar cells (APTSCs), which is formed by combining two perovskite-based sub-cells with different bandgaps into a monolithically stacked structure. This tandem structure allows the solar cell to absorb different components of sunlight within the two absorber layers, extracting on average more useable energy per photon absorbed. Consequently, tandem solar cells can achieve a power conversion efficiency (PCE) above that of a single-junction solar cell, the limiting efficiency of which is marked by the single-junction radiative limit.[2] To most effectively implement this concept, the monolithic APTSCs usually consist of a narrow (≈1.20 eV) and a wide (≈1.80 eV) E_g perovskite for the bottom and top subcells,[3] respectively. APTSCs have been reported with PCEs of 28.0%, i.e., well beyond 25.7% PCE of the current record single-junction perovskite solar cell (PSC).[4,5]

This study concerns the bottom cell of APTSCs, which uses a narrow bandgap perovskite film as the light absorber. Mixing tin (Sn) and lead (Pb) as the B-site cation is required to achieve a sufficiently small E_g.[6] Sn-Pb perovskites reach a minimum E_g of ≈1.20 eV when the ratio of Sn to Pb is about

F. Yang, R. W. MacQueen, D. Menzel, A. Musiienko, A. Al-Ashouri, K. Prashanthan, D. Abou-Ras, L. Korte, I. Levine, S. Albrecht
Division Solar Energy
Helmholtz-Zentrum Berlin für Materialien und Energie GmbH
12489 Berlin, Germany
E-mail: fengjiu.yang@helmholtz-berlin.de; igal.levine@helmholtz-berlin.de; steve.albrecht@helmholtz-berlin.de

The ORCID identification number(s) for the author(s) of this article can be found under https://doi.org/10.1002/aenm.202204339.

DOI: 10.1002/aenm.202204339

J. Thiesbrummel, H. Snaith
Clarendon Laboratory
University of Oxford
OX1 3PU Oxford, United Kingdom

S. Shah, M. Stolterfoht, D. Neher
Institute of Physics and Astronomy
University of Potsdam
14476 Potsdam-Golm, Germany

K. Prashanthan
Department of Physics
University of Jaffna
Jaffna JA 40000, Sri Lanka

S. Albrecht
Faculty of Electrical Engineering and Computer Science
Technische Universität Berlin
10587 Berlin, Germany

1:1.[7,8] Substantial efforts have been invested into improving the photovoltaic (PV) performance of mixed Sn-Pb perovskites that contain methylammonium (MA) as the main A-site cation, improving the crystallinity, suppressing oxidation of Sn^{2+}, prolonging carrier lifetime and diffusion length, and reducing trap density. The use of additives is the most common approach to improve the optoelectronic properties of the Sn-Pb perovskite, employing chloride anions, guanidinium thiocyanate (GuaSCN), metallic Sn powder, cesium ions (Cs^+), formamidine sulfinic acid (FSA), ammonium-cation, 4-trifuoromethylphenylammonium, and mixed phenethylammonium (PEA^+) and guanidinium (Gua^+).[9–15] The ammonium-cation, 4-trifuoromethyl-phenylammonium, was introduced into Sn-Pb perovskite precursors. This not only improved the properties of the perovskite films and crystals, but also allowed to increase the thickness of perovskite films up to 1.20 µm, resulting in PCEs of 22.2% and 26.4% for single-junction and APTSCs,[14] respectively. Mixed organic cations of phenethylammonium and guanidinium were introduced into perovskite precursors to form a quasi-two-dimensional structure consisting of $(PEA)_2GAPb_2I_7$ on the pristine perovskite surface. As a result, the bulk carrier lifetime and surface recombination velocity were increased to ≈9.2 µs and reduced to ≈1.4 cms^{-1}, respectively. With this, the V_{OC} of the single-junction device was increased to 0.916 V.[15] Post-treatment is another approach to improve the optoelectronic properties of the Sn-Pb perovskite surface, employing molecules phenethylammonium iodide (PEAI), ethylenediamine (EDA), and glycine hydrochloride (GlyHCl) and ethylenediammonium diiodide ($EDAI_2$).[16–18] To address the high trap density between the perovskite and hole transport material (HTM), GlyHCl and $EDAI_2$ were introduced into perovskite precursors and posttreatment agents, facilitating passivation of both surfaces of the perovskite film, leading to oriented interface aggregates of the molecules, and surface dipoles formation for improved charge extraction. The improved perovskite generated record PCEs of 23.6% and 21.0% for PSCs on 0.1 and 1.0 cm^2 aperture areas,[18] respectively.

Alkali metal salts such as rubidium iodide (RbI) and potassium iodide (KI) were used as doping agents in MA-containing Sn-Pb perovskite to improve crystallinity and carrier lifetime, and reduce recombination resistance.[19] However, the working mechanism of these alkali metal salts, such as their physical distribution within the film, their interaction with Sn vacancies, and their effect on interface and bulk recombination is not yet well-understood. Deeper insight into these processes may allow further improvements in PSCs performance through rational design of the treatment schemes, which is one of the goals of this study.

We elected to use a perovskite formulation free from the MA cation in this study. MA-free perovskites can achieve better stability compared to MA-containing pure Pb-PSCs.[20–23] However, research efforts into MA-free mixed Sn-Pb perovskite lag far behind that of MA-containing compositions. Previous studies included the perovskite composition modification regarding the Sn to Pb ratio, in-situ passivation by FSA, HTL modification by hexaazatrinaphthylene, post-treatment by PEAI, and gas-quenching for perovskite crystallization. [8,24–27] The first report of MA-free Sn-Pb PSCs showing PV performance comparable with a MA-containing composition was by Werner et al., who employed a gas quenching process for the formation of perovskite film and a poly[bis(4-phenyl)(2,4,6-trimethylphenyl)amine] (PTAA) HTM.[27] The gas quenching improved the crystallinity of the Sn-Pb perovskite with larger grain sizes, better crystal orientation, and greater phase purity compared with a recipe that used diethyl-ether antisolvent. This report marked the first time that MA-free Sn-Pb PSCs achieved 20% PCE, and the devices maintained 80% of their initial efficiency after 4000 h with thermal stress of 85°C under open-circuit and dark conditions. In addition, the MA-free Sn-Pb was applied in APTSCs, and gained an impressive efficiency of 26.3% when indium tin oxide nanocrystals were employed as hole transport material (HTL) to replace poly(3,4-ethylenedioxythiophene) polystyrene sulfonate (PEDOT:PSS).[28] Despite these promising developments, MA-free Sn-Pb perovskites still lag behind MA-containing Sn-Pb perovskites in terms of performance and research intensity.

Herein, we systematically investigated the structural and optoelectronic properties, as well as the solar cell performance, of the MA-free perovskite $FA_{0.83}Cs_{0.17}Sn_{0.5}Pb_{0.5}I_3$ with introduction of the alkali metal salt RbI as an additive to the perovskite precursors. We found that the RbI additive caused a redistribution of the elements within the film, resulting in a new composition of $FA_{0.83}Cs_{0.17-x}Rb_xSn_{0.5}Pb_{0.5}I_3$. This new composition exhibited a change in the lattice strain, and a compositional gradient from the film surface into the bulk. Quasi-Fermi level splitting (QFLS) and transient photoluminescence (trPL) measurements were carried out repeatedly for several days after sample preparation, and we could demonstrate pronounced increase in QFLS, PL lifetime, and device performance. Reference and RbI additive samples both showed an improvement in performance after one week of storage (the reference did not contain RbI in the precursor solution). The RbI-containing perovskite achieved a peak QFLS of 0.925 eV after one-week storage compared with 0.890 eV for the reference on the quartz substrates. The nonradiative recombination losses at the perovskite/C_{60} and perovskite/PEDOT:PSS interfaces were lower in the samples with RbI-containing perovskites. Additionally, the carrier lifetime on quartz substrates was significantly greater for the RbI-containing perovskite, increasing from 1.46 µs in the reference to 9.46 µs in the RbI sample. In order to understand the mechanism responsible for the superior performance of the RbI-containing perovskite, highly sensitive photoelectron yield spectroscopy measurements in constant final state (CFSYS)[29,30] were performed, revealing a ten-fold reduction in the surface defect density. Additionally, Hall effect measurements indicated nearly two orders of magnitude lower hole carrier concentration, and increased resistivity in the RbI-containing sample compared to the reference. The raised Fermi-level resulting from RbI incorporation rendered the perovskite more intrinsic. Together, these improvements yielded MA-free Sn-Pb PSCs with over 20% PCE and 0.823 V V_{OC} compared to the reference device (18.32% PCE and 0.762 V V_{OC}). Furthermore, the RbI also reduced the hysteresis and current loss induced by mobile ions. Our systematic study provides important new insights for accelerating the progress of MA-free Sn-Pb perovskites for high-performance single-junction solar cells and APTSCs.

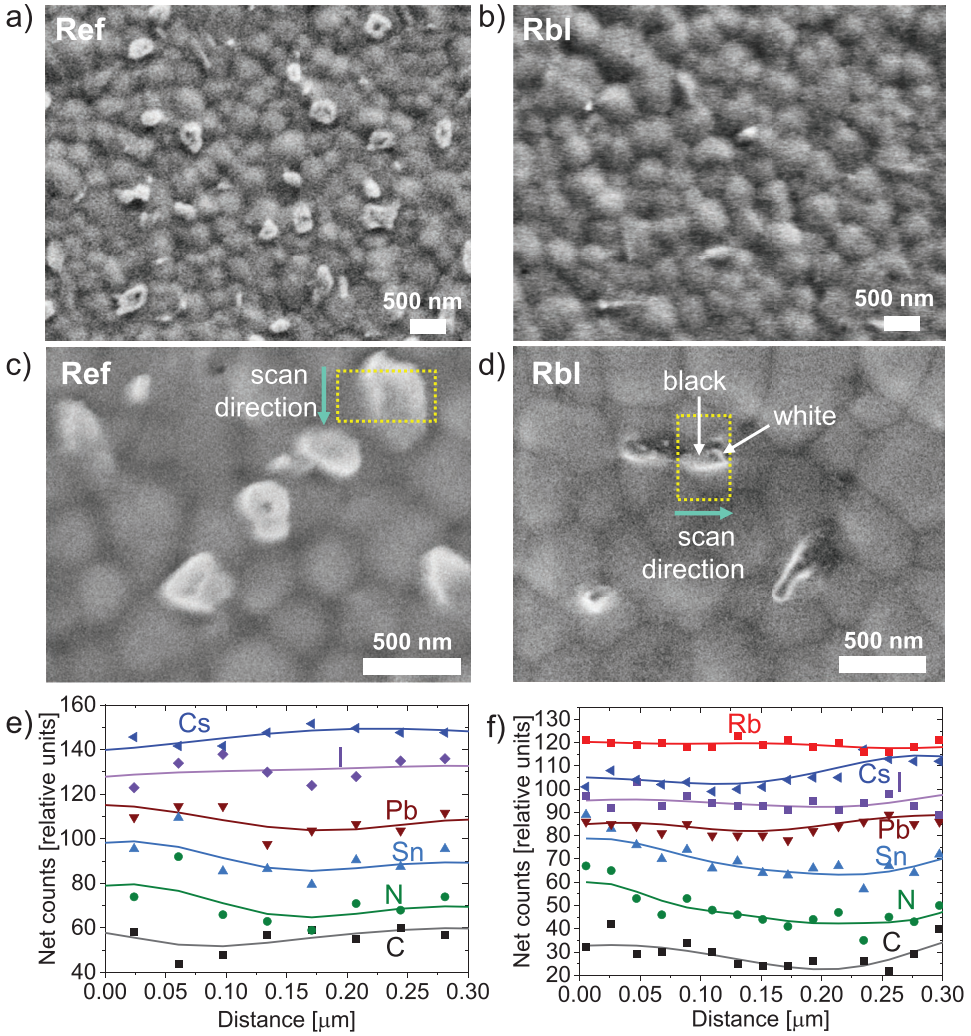

Figure 1. Surface morphology characterization of MA-free Sn-Pb perovskites. a,b) SEM images of the reference (Ref) and RbI-containing Sn-Pb perovskite films' surface morphology. c,d) Line scan analysis of the precipitates on the perovskite surfaces. The dashed area was selected for the line scan integrated area: lengths are lines of the integration window, and the widths are line-scans. The green arrow is the scanning direction. The scale bar is 500 nm. e,f) Line scan analysis summary of the reference (Ref) and RbI-containing perovskites.

2. Results and Discussion

2.1. Analysis of Surface Morphologies and Compositions

The MA-free Sn-Pb perovskite $FA_{0.83}Cs_{0.17-x}Rb_xSn_{0.5}Pb_{0.5}I_3$ (henceforth denoted "RbI-perovskite") was studied alongside a reference material which contained no RbI ($x = 0$, denoted "Ref"). A 3.5% molar ratio of the RbI additive was used for the Sn-Pb perovskite films. First, the surface morphology of the perovskite films was investigated using scanning electron microscopy (SEM), as shown in **Figure 1**a,b. The surface of the reference sample was covered with large-grained precipitates with surface coverage of ≈10%. In the RbI-containing perovskite, the surface coverage by precipitates was reduced to ≈2%. The average grain size increased from ≈300 nm in the reference to ≈600 nm in the RbI-containing perovskite sample with a distribution ranging up to 800 nm, as shown in the histogram in Figure S1, Supporting Information. Larger grains may contribute to the lower recombination rate of the RbI-containing sample (vide infra) since grain boundaries can be regions of enhanced non-radiative recombination.[31,32]

To understand the composition of the surface precipitates, energy-dispersive X-ray spectroscopy (EDX) measurements were used to analyze two magnified areas of the perovskite film. EDX mapping was first conducted to analyze the element distribution of the reference and RbI-containing samples, as shown in Figure S2, Supporting Information. To gain deeper insight into the elemental composition of precipitates, the aggregated linescans were calculated from EDX elemental distribution maps in the directions indicated by the green arrows, as showed the dashed rectangular areas in Figure 1c,d. The precipitates visible in the reference sample consist likely of CsI, because only the signals of Cs and I were enhanced on the analyzed precipitate, as shown in Figure 1e. The signals of the other elements (Pb, Sn, N, and C) were reduced.

In contrast, for the RbI sample, the signals of Rb and I were slightly enhanced as compared with those of Pb, Sn, N, and C at the beginning of the linescan, suggesting the presence of RbI on the surface. Then, the Cs and I signals were enhanced in the further course of the linescan while the Rb signal was reduced slightly, as shown in Figure 1f. From this behavior, we infer that the RbI-containing perovskite surface has a slightly different composition with smaller CsI precipitates compared with the reference. This finding is different from previous reports where the RbI was used in MA-containing Sn-Pb perovskite as a doping agent, and it only changed the film's compactness and grain sizes.[19] This indicates that in our case, a new perovskite composition of $FA_{0.83}Cs_{0.17-x}Rb_xSn_{0.5}Pb_{0.5}I_3$ might be formed, together with a Cs-related compound. These changed surface features of the RbI-containing perovskite are also different to the effects of other additives in Sn-Pb perovskites.[9,10,12–15,17–19,24]

2.2. Evaluation of Crystalline and Elemental Distribution

X-ray diffraction (XRD) characterization was applied to understand the effect of RbI on the crystallinity of the Sn-Pb perovskites on PEDOT:PSS/ITO (Indium-Tin-Oxide, ITO) glass substrate. As shown in **Figure 2**a, the crystal phase of the perovskite did not change after adding RbI. The intensity ratio of the peaks associated with the 110 and 220 reflections decreased from 1.11 to 1.07 after adding RbI, signifying a slight change in the orientation of the crystals and the Sn-Pb perovskite becoming more uniform and less micro-strained according to the Williamson–Hall plot.[19,33] The main diffraction peaks of perovskite shifted to smaller angles with the addition of RbI, including 110, 202, 220, 310, and 224, as shown in Figure 2b–f, signifying that the Rb ions might be embedded into the crystal.[34] These effects may improve the resistance of Sn (II) towards oxidation with lower defect densities on the surface and in the bulk as a result.[12]

Secondary-ion mass spectrometry (SIMS) was then employed to investigate the depth profile of Rb, as shown in Figures 2g,h and Figure S3, Supporting Information. Perovskite samples were fabricated on glass/ITO/PEDOT:PSS substrates. The thickness of the perovskite layers was ≈500 nm with a perovskite precursor concentration of 1.4 M. In the reference sample, the elements Cs, Pb, Sn, and I were uniformly distributed from the surface to the bulk, exhibiting a flat distribution. At a depth of ≈0.5 µm, a peak in intensity appears concomitantly for sulfur (S) and fluorine (F) (Figure S3a, Supporting Information). This marked the transition region from the perovskite and PEDOT:PSS region to ITO, which was clearly assignable

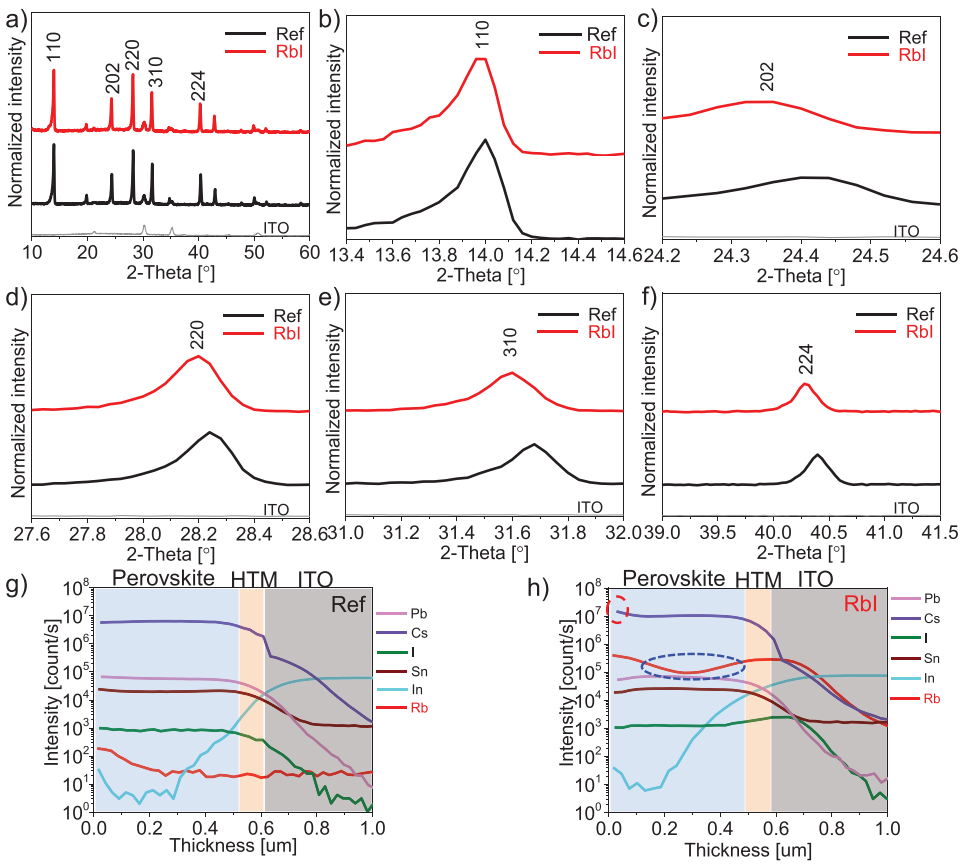

Figure 2. a) XRD patterns of reference (Ref) and RbI-containing perovskites on glass/ITO/PEDOT:PSS substrates. b–f) Zoomed XRD patterns of the reference (Ref) and RbI-containing samples at the diffraction positions of 14°, 24.4°, 28.3°, 31.7°, and 40.4°, respectively. g,h) Elemental depth profiling by secondary-ion mass spectrometry (SIMS) measurements of reference (Ref) and RbI-containing perovskite films on the glass/ITO/PEDOT:PSS substrates. Depth regions with predominant contributions from the perovskite, PEDOT:PSS, and ITO have been marked as a guide to the eye.

due to the appearance of the S signal. Of interest was the distribution of fluorine (F), which originates from the SnF_2, where the F was mainly accumulated at the interface between perovskite and PEDOT:PSS as previously reported.[18] However, the fluctuation of the F signal near the surface of the reference sample was much larger than in the RbI-containing sample (Figure S3b, Supporting Information), indicating that the RbI additive modified the distribution of SnF_2. Other than that, in the RbI-containing sample, most of the elemental distributions were similar to those of the reference with small deviations for Pb and Sn and different behavior for the Cs, I, and Rb. While for the reference, Pb and Sn showed a flat distribution from the perovskite surface to the bulk, a slight decrease in intensity was observed for these elements towards the surface of the RbI-containing perovskite. The Cs exhibited a graded distribution from surface to bulk, suggesting that Cs atoms had an enriched concentration at the perovskite surface as a result of RbI additive, consistent with the observations in EDX line-scans and mapping. The Rb distribution showed a valley situated within the perovskite bulk, demonstrating that Rb was distributed through the whole perovskite film but with preferential accumulation at the surface and at the interface to the substrate. Additionally, the distribution of I somewhat followed that of Rb, with a peak in prevalence at the perovskite/PEDOT:PSS interface, but an otherwise flat distribution throughout the surface and bulk of the perovskite. In summary, we found a Rb accumulation at both perovskite surfaces when using the RbI additive. This contrasts with a previous report that the GylHCl was used as an additive to passivate the perovskite/HTM interface, and $EDAI_2$ was employed as a post-treatment agent at the interface of perovskite/C_{60} in the same study.[18]

2.3. Characterization of Optical Properties, Nonradiative Recombination Losses, Carrier Lifetime, and Defect Density

Optical characterization helped us to further assess the working mechanism of the RbI additive. All absorption and photoluminescence (PL) spectra were measured with the excitation light incident on the glass substrate side, as shown in Figure S4a. All the samples were encapsulated before PL characterization, as shown in Figure S4b, Supporting Information. The bandgap energy was determined from Tauc-plots,[35] and was ≈1.265 eV in the reference and RbI-containing samples, as shown in the inset figure of **Figure 3**a. Slightly reduced absorption above the band gap energy in the RbI-containing sample might be due to the accumulation of Rb and Cs atoms on the surface. The PL intensity of the perovskite was significantly increased after using the RbI while the emission position remained unchanged at 1.260 eV, conforming the bandgap from the Tauc-plot evaluation, as shown in Figure S5a, Supporting Information.

To gain insight into the nonradiative recombination losses of two sample types, quasi-Fermi level splitting (QFLS) measurements were carried out by acquiring absolute steady-state PL spectra. The QFLS can be calculated from steady-state PL quantum yield according to procedure reported by Ross et al.,[36] using the equation $QFLS = k_B \ln (J_{SC}/J_0) + k_B T \ln(PLQY)$ (k_B: Planck constant; T: temperature; PLQY: PL quantum yield;). As displayed in Figure 3b and Table S1, Supporting Information, the QFLS values were improved by the RbI additive, both with and without the presence of C_{60} and PEDOT:PSS as the charge carrier extraction materials (CTMs). The QFLS of the neat perovskite on quartz increased significantly with RbI additive, from 0.872 to 0.918 eV on average, indicating that the non-radiative recombination losses of the perovskite were suppressed significantly by RbI. After combining with PEDOT:PSS, the QFLS value of the reference sample was reduced remarkably to 0.697 eV on average, i.e., a loss of 0.175 eV, while the QFLS was 0.794 eV on average for the RbI-containing perovskite with HTM, i.e., a loss of 0.124 eV. The RbI additive hence evidently reduced the recombination losses at the perovskite/PEDOT:PSS interface, allowing for higher potential open-circuit voltage (V_{OC}). For the perovskite/C_{60} interface, the RbI-containing sample likewise had higher QFLS compared with the reference, although the magnitude of the QFLS reduction induced by the C_{60} was only slightly larger than in the reference. Finally, the QFLS of a full solar cell layer stack without rear metal electrode, i.e., structure glass/ITO/PEDOT:PSS/perovskite/C_{60}, was measured for both perovskite types. The RbI-containing sample exhibited a higher QFLS value of 0.800 eV compared with 0.788 eV of the reference on average, which implied that the RbI-containing PSCs would have a higher V_{OC} potential.

Interestingly, the QFLS values of reference and RbI-containing samples improved after one week of storage in the nitrogen-filled glovebox, before stabilizing in the second week of storage and gradually diminishing in the third week. The QFLS values of the bare RbI-containing perovskite and full simulated solar cell layer stack were increased to a maximum of 0.925 and 0.847 eV on average, respectively. These values are higher than the previously reported value for Sn-Pb perovskites.[37] Overall, the recombination losses at the PEDOT:PSS/perovskite interface are still the main challenge for the Sn-Pb perovskites, and it is important to develop HTMs with less recombination losses, such as the self-assembled monolayers utilized with pure lead perovskites.[38,39]

The PL intensity and photostability of Sn-Pb perovskites improved upon continuous illumination by PL excitation light for 23 min before and after one week of storage in the glovebox, as shown in Figure S5b–f, Supporting Information, has been similarly observed in previous reports.[40,41] The RbI-containing sample had much better photostability compared with the reference. We also evaluated the air stability of Sn-Pb perovskite by recording the absolute PL without encapsulation, as shown in Figure S6a,b, Supporting Information. The QFLS values of the unencapsulated perovskites had a similar trend compared with the encapsulated samples, and the RbI-containing sample still showed a QFLS of 0.895 eV after one week on the quartz substrate. In addition, the photostability of perovskite films without encapsulation was also acquired after one-week storage in air, as shown in Figure S6c–e, Supporting Information. The RbI-containing sample kept better photostability compared to the reference. To sum this up, we showed that the RbI additive strongly improved the perovskites' air stability and suppressed recombination losses in the bulk and at interfaces.

To better understand the enhanced electronic properties of the MA-free Sn-Pb perovskite after prolonged storage, trPL and QFLS measurements of a set of samples were conducted

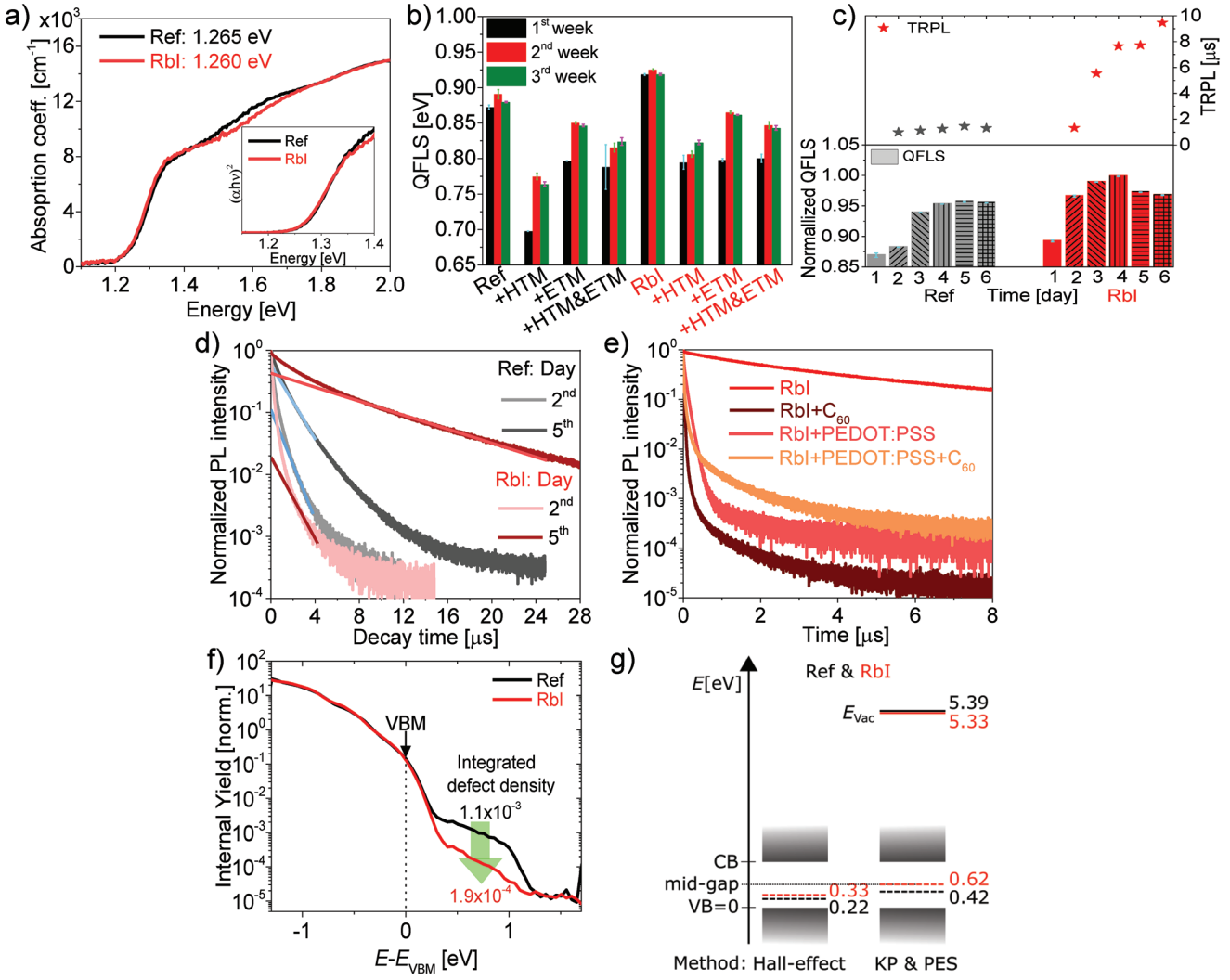

Figure 3. a) Absorbance spectra and Tauc-plots of perovskites without and with RbI additive, respectively. Black: reference (Ref) perovskite, red: perovskite with RbI additive. b) QFLS values of perovskites with various carrier transport materials measured on the 1st, 2nd, and 3rd week of storage in a nitrogen-filled glovebox after fabrication. Samples "Ref" and "+ETM" (black), "RbI" and "+ETM" (red) were fabricated on quartz substrates with electron transport material (ETM). The "+ETM" denotes evaporated C_{60} on the reference (Ref) and RbI-containing perovskites surfaces. "+HTM" denotes the perovskite films fabricated on the ITO/PEDOT:PSS with PEDOT:PSS acting as HTM. "+HTM&ETM" denotes preparation on a glass/ITO/PEDOT:PSS HTM substrate with evaporated C_{60} ETM on the perovskite surface. The error bar of QFLS values is included. c) Normalized QFLS values (lower panel) and absolute carrier lifetimes (upper panel) for stored samples (increasing time between preparation and measurement). To compensate for measurement errors from misalignment between light source and mask for the QFLS measurement, the final value of QFLS was normalized by the maximum value of the RbI sample during the day-to-day measurement, as shown in Table S2, Supporting Information. d) Comparison of the transient PL (trPL) measurements of the reference (Ref) and RbI-containing perovskites on quartz substrates on the 2nd and 5th day of storage in a nitrogen-filled glovebox after fabrication. e) TrPL transients of the RbI-containing perovskite on quartz with and without C_{60}, PEDOT:PSS, and C_{60} plus PEDOT:PSS HTM. f) Photoelectron yield spectroscopy in constant final state (CFSYS) spectra of glass/ITO/PEDOT:PSS/perovskite samples. The valence band maximum, VBM, and occupied gap states (green arrow; label: normalized integrated defect densities) are indicated. Cf. ref. [29] for details of the CFSYS method and data analysis. g) Comparison of energetic levels in reference (Ref) and RbI-containing perovskites. Dashed lines: Fermi-level positions. The Fermi-level position on the left side is determined by Hall-effect measurements. The energetic positions on the right side are determined by a combination of near-UV photoelectron spectroscopy (to obtain ionization energies, i.e., E_V–E_{Vac}) and Kelvin probe (to obtain the work function, i.e., E_F–E_{Vac}) measurements.

over six sequential days of storage, with samples stored in the nitrogen-filled glovebox in between measurements. To ensure the measurement was made on the same point of the sample surface, a shadow mask with a 0.4 cm diameter hole was glued to each substrate prior to the first measurement, with the opening located in the middle of the perovskite film. The hole size was chosen to be slightly larger than the PL laser spot size. Figure 3c shows normalized QFLS and absolute carrier lifetime (τ) values of the neat perovskite samples on the quartz substrates, plotted as a function of sample storage time measured in days. The evolution in QFLS values of the reference sample were consistent with the carrier lifetime measurements. The

average values (three measured positions of the sample) of the QFLS reached a maximum on the 5th day, where a carrier lifetime of 1.46 µs was obtained, as shown in Tables S2 and S3, Supporting Information. Then, both QFLS and τ decreased after the 6th day. For the RbI-containing sample, the trends of QFLS and lifetime deviate: the QFLS value increased significantly on the 2nd day and then reached a maximum value on the 4th day. Interestingly, the carrier lifetime was dramatically enhanced from the 3rd day and reached a maximum of 9.46 µs on the 6th day, which was longer than the MA-containing Sn-Pb perovskites,[15] and other reported values.[8,9,11–17,23–26,30,33,35] Figure 3d shows a comparison of the trPL transients of the reference and RbI-containing samples on the 2nd and 5th day. The trPL decays of the reference sample were almost identical on the 2nd day and 5th day and stayed comparably short. However, the trPL decays of the RbI-containing sample became substantially long on the 5th day, and much longer than the reference sample. The trPL transients of the perovskites on the intermediate days are also shown in Figure S7a,b, Supporting Information.

The trPL transients of the perovskites with CTMs of PEDOT:PSS and C_{60} were also characterized, as shown in Figure 3e and Figure S7c–f, Supporting Information. The trPL transients of the RbI-containing perovskite had a faster initial decay compared with the reference (Figure S5d, Supporting Information) after combining with C_{60}, suggesting that electron extraction into the C_{60} was improved for the perovskite with RbI additive. At longer times the transient still decayed slowly and the QFLS was higher than for the reference in contact with C_{60}. In contrast, the carrier extraction became slightly slower for the RbI-containing sample compared with the reference sample after combining with PEDOT:PSS, as shown in Figure S7e, Supporting Information. This indicates a bottleneck for hole extraction, meaning that optimizing the interface to the PEDOT:PSS or finding better alternative HTLs could substantially enhance the PV performance. Contacted with both PEDOT:PSS and C_{60}, the RbI-containing perovskite showed a faster carrier extraction than the reference sample again (Figure S7f, Supporting Information). These results reinforce the importance of developing more efficient HTMs for Sn-Pb perovskites.

To gain a more detailed insight into the non-radiative recombination losses versus charge extraction, the differential lifetime $\tau = -\{d \ln[\phi(t)]/dt\}^{-1}$ was calculated from the transient PL (Figure S7g–i, Supporting Information), where the $\phi(t)$ is the time-dependent PL photon flux. Through this, the decay time becomes available for each point in time during the transient, and different processes can thus be differentiated.[42] As simulated by Krogmeier et al.,[42] the transition between the charge carrier extraction processes and trap-assisted recombination at the early stage ($\tau < 1.0$ µs) can be discerned by a sharp rise of the differential lifetime. As discussed above, the carrier extraction is accelerated at the C_{60} interface (quartz/perovskite/C_{60} sample) and in the case with both PEDOT:PSS and C_{60}, followed by a larger decay time of the RbI-containing perovskites that indicates a lower trap density.

Near-UV photoelectron spectroscopy with varying excitation energy in constant final state mode (CFSYS) was carried out on the Sn-Pb perovskites in a layer stack of glass/ITO/PEDOT:PSS/perovskite. CFSYS enables a direct measurement of the density of occupied states in the valence band region as well as in the band gap up to the Fermi edge with a large dynamic range. Furthermore, standard ultraviolet photoelectron spectroscopy (UPS) measurements with a constant excitation energy of 6.5 eV were performed to investigate the work function (WF) and thereby determine the ionization energy. The CFSYS spectra were modeled based on a band-fluctuation model relying on the assumption of a parabolic band edge, which was previously adapted for Pb-based perovskite compositions,[29] as shown in Figure S8, Supporting Information. The density of occupied defects in the bandgap is modeled by three Gaussian distributions included in the combined model of the spectra. Note that due to the broad defect distribution, this choice is somewhat arbitrary, and we will therefore refrain from assigning any deeper physical meaning, e.g., to the energetic positions of the Gaussians.

To directly compare the density of occupied defects of the reference and RbI-containing perovskites, the measured CFSYS spectra were aligned at the valence band maximum (VBM) and normalized to the internal photoelectron yield (which is proportional to the density of states), as shown in Figure 3f. We found that the RbI additive significantly reduced the integrated density of defect states by around one order of magnitude. Note, the information depth of these near-UV photoelectron spectroscopy (PES) techniques is limited to 5–10 nm. However, as the nonradiative recombination processes are usually dominated by the surfaces/interfaces of the layer stack, CFSYS can provide valuable information about the origin of the nonradiative recombination in a very direct manner. Here, we show clear evidence that the strongly improved carrier lifetime of the RbI-containing perovskite can be explained by a substantially reduced defect density at the perovskite surface.

In combination with UPS, we can obtain the ionization energy. The Fermi level at the surface can largely deviate from the one of the ITO, being the conductive substrate, due to surface photovoltage effects, which makes a reliable determination of its position in the bandgap not straightforward.[30] However, the ionization energy is independent of the Fermi level position in the band gap, and can hence still be obtained by the WF and VBM both evaluated with respect to the contacted Fermi level of the ITO as in Figure S8, Supporting Information and **Table 1**. The obtained values of −5.33 and −5.39 eV indicated no significant effect of the RbI additive on the ionization energy, considering the experimental error of 0.07 eV. This is in line with the XRD measurements mentioned above, which do not indicate any significant structural change in the perovskite itself.

The WF of the perovskite film was determined by Kelvin probe (KP) was shifted from 4.97 eV in the reference to 4.71 eV in the RbI-containing sample. These values, combined with the

Table 1. Energetic positions determined by photoelectron spectroscopy (PES), Kelvin Probe (KP) of perovskite films without and with RbI additive.

	Ionization energy (eV)	WF (eV)	E_F–E_V (eV)
Method	PES	KP	PES&KP
Ref	5.39	4.97	0.42
RbI	5.33	4.71	0.62

Table 2. Results from AC Hall-effect measurements of Sn-Pb perovskites with and without RbI additive.

	Type of conductivity	Resistivity (Ω cm)	Concentration (p, cm^{-3})	Hall mobility ($cm^2\ V^{-1}\ s^{-1}$)	VBM (E_v–E_f) (eV)	Increased resistivity ratio	Reduction hole concentration
Ref	*p*-type	6.2×10^3	5.7×10^{14}	1.78	0.22	–	–
RbI	*p*-type	4.7×10^5	7.8×10^{12}	1.71	0.33	76	72

ionization energies obtained from the PES measurements, indicated E_F-E_V values of 0.42 and 0.62 eV for the reference and RbI-containing samples, respectively, as summarized in Table 1. This suggested that the RbI additive effectively de-doped the perovskite, to become less *p*-type and more intrinsic. The resulting energy level diagram of the Sn-Pb perovskites is depicted in Figure 3f. The shifted VBM of the RbI-perovskite resulted in improved energy level alignment with PEDOT:PSS (–5.2 eV).[12] However, the offset between the conduction band minimum of the perovskite and C_{60} lowest unoccupied molecular orbital (LUMO) was much larger in the RbI-containing sample compared to the previous reports.[12,43] It should be considered that both PES and KP data only provide information about the sample surface. Therefore, to corroborate this conclusion, Hall-effect measurements with alternating (AC) magnetic field were used to further characterize the Sn-Pb perovskites' bulk. AC Hall-effect measurements provide a high signal-to-noise ratio, which allows studying charge transport in highly-resistive perovskite thin films that are hardly resolvable in a constant magnetic field regime. As shown in **Table 2**, the reference and RbI-containing perovskite films both exhibited *p*-type conductivity in the order of $>10^{12}$ cm^{-3} level hole carrier concentration, which implied that the holes were the majority carrier. However, the hole concentration of the RbI-containing sample was almost two orders of magnitude lower compared with the reference. This probably indicates that Sn (IV) vacancy formation was suppressed significantly by the RbI additive,[11,13,14,18,26,31] and is consistent with the increased E_F–E_V value at the surface which was found with the PES and KP measurements. Consequently, the resistivity also increased by a similar value for samples with the RbI additive. The different hole concentrations obtained from the Hall measurements can also be used to calculate the E_F.–E_V values for the perovskites' bulk (see the Supporting Information for more details), resulting in values of 0.22 and 0.33 eV for the reference and RbI-containing samples, respectively. Thus, although the absolute values of E_F–E_V were different from those shown in Table 1 (which we attributed to the different sensitivity to bulk vs surface), the overall trend was the same, as shown in Figure 3f, pointing to more intrinsic perovskite following the RbI treatment. The concomitant increase of electron concentration, thus conductivity for this carrier type, should also improve carrier extraction at the electron contact.

2.4. Investigations in Solar Cell Devices

The aforementioned evidence of perovskite properties, especially the enhanced carrier lifetime due to significantly reduced defect density with RbI, indicates that the PV performance of Sn-Pb PSCs should be improved with RbI additive, which we found to be true in practice. Figure S9, Supporting Information, shows the architecture of the fabricated Sn-Pb PSCs, including the glass/ITO substrate, PEDOT:PSS HTM, $FA_{0.83}Cs_{0.17-x}Rb_xSn_{0.5}Pb_{0.5}I_3$ absorber, C_{60} ETM, bathocuproine (BCP), and copper (Cu) electrode. Cross-sectional SEM images are shown in Figure S10. The reference and RbI devices had a perovskite absorber with a similar thickness of ≈500 nm, and a 40 nm thick PEDOT:PSS HTM. The crystal morphology was slightly different because of the RbI additive, as previously discussed.

Various concentrations of the RbI additive were investigated to elucidate the RbI concentration dependence of device performance. As shown in Figure S11, Supporting Information, the V_{OC} of PSCs gradually improved as the RbI concentration increased, reaching a maximum value when the concentration was 3.5%, which is in the line with our above investigation. The V_{OC} decreased again when the concentration exceeded 3.5%, but still remained higher than in the reference PSCs. The fill factor (FF) was slightly enhanced as the RbI concentration increased and then dropped significantly at concentrations above 3.5%, which might be due to Rb and Cs accumulation at the perovskite surface, diminishing the surface conductivity of the perovskite. Overall, addition of 3.5% RbI achieved the highest PCE of 17.24% on average.

To produce our best-performing PSCs, a lengthy (more than 5 hours) nitrogen purge of the glovebox was carried out directly prior to device fabrication to clean the glovebox atmosphere. The current density-voltage (*J-V*) curves of those best-performing PSCs are exhibited in **Figure 4**a. A measurement aperture of 0.10 cm^2 was used. The RbI PSCs generated a higher V_{OC} of 0.823 V (0.817 V), a FF of 77.8% (75.0%), and a 20.12% (19.24%) PCE in reverse (forward) compared with those of the reference device with 0.762 V (0.757 V) V_{OC}, 76.8% (72.7%) FF, and 18.32% (17.01%) PCE in reverse (forward). To our knowledge, this result marks – next to the nitrogen gas quenching with 20% PCE[27] – the first report of MA-free Sn-Pb PSCs with PCE greater than 20%[8,24–28,44] enabled by the RbI additive. The RbI additive additionally reduced hysteresis during *J–V* measurements. To demonstrate the high V_{OC} of the PSCs with the addition of RbI, measurements without an aperture were also carried out. The V_{OC} of the RbI PSC reached 0.842 V with a 20.35% PCE and small hysteresis, as shown in Figure S12a, which is the highest V_{OC} reported for MA-free Sn-Pb PSCs.[8,24–27,44]

The integrated current density of both PSCs was verified by external quantum efficiency measurements, as shown in Figure 4b. The integrated current density was within 2% deviation of the short-circuit current density (J_{SC}). The short-term maximum power point (MPP) output was measured and is displayed in Figure 4c. The RbI-containing PSC had a higher MPP efficiency compared with the reference and sustained

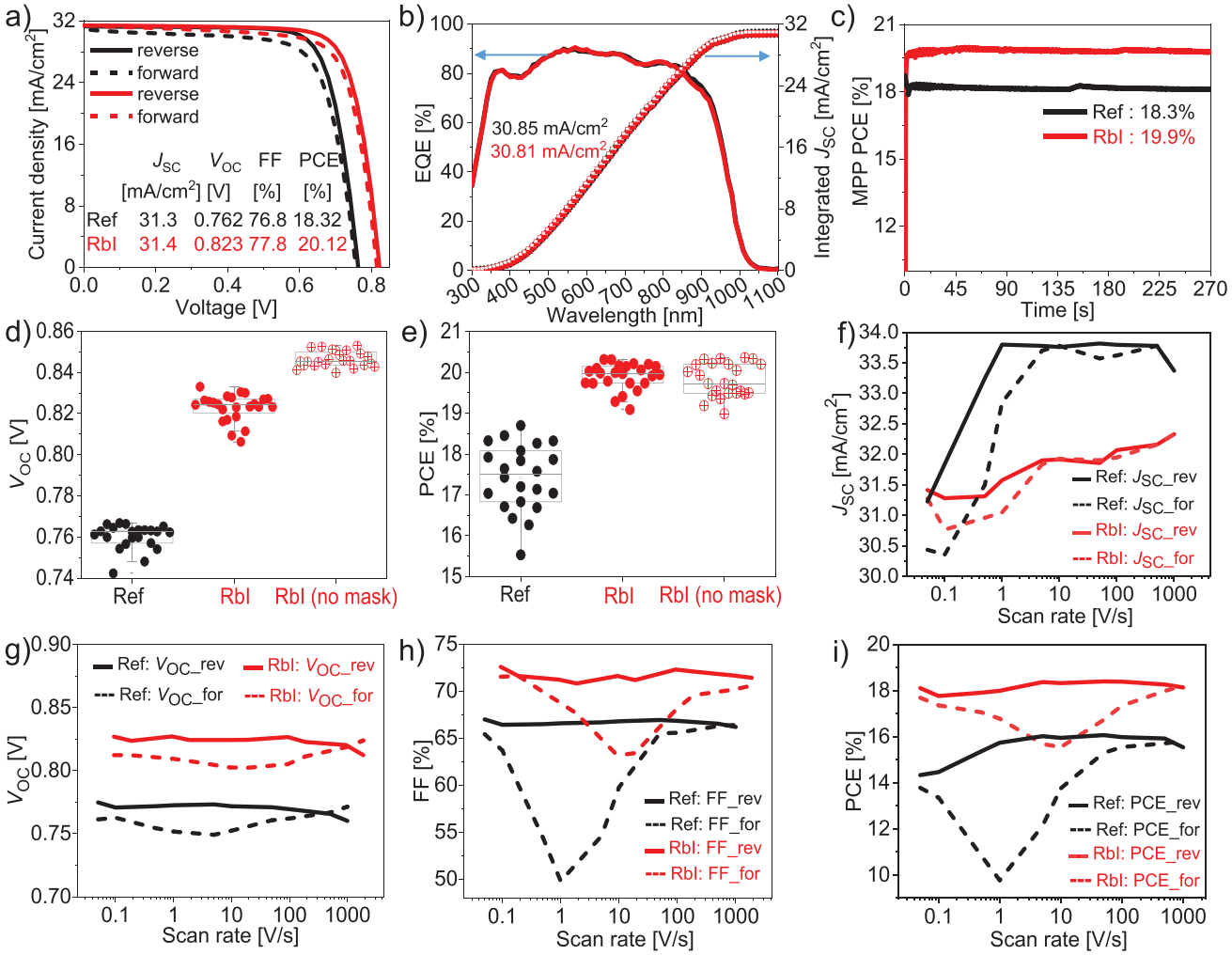

Figure 4. *J–V* curves and PV parameters of Sn-Pb PSCs with and without RbI additive. The active area was defined by a 0.10 cm^2 aperture mask. b) EQE spectra of reference (Ref) and RbI-containing PSCs. c) MPP tracking of reference (Ref) and RbI-containing PSCs for 270 s. d,e) V_{OC} and PCE distributions of reference (Ref) and RbI-containing PSCs with measurement aperture, and without aperture (for RbI-containing PSCs). RbI(no mask) implies the active area of the solar cell is 0.18 cm^2 without masking during the *J–V* scanning. f–i) Fast hysteresis measurement of the reference (Ref) and RbI-containing PSCs, including J_{SC}, V_{OC}, FF, and PCE. The active area was defined by a 0.10 cm^2 aperture mask.

a stable value during the 270 s measurement. We also tested longer-duration MPP stability of PSCs, and the RbI-containing device had similar stability compared with the reference within 18 hours, as shown in Figure S11b, Supporting Information, which indicated that the RbI additive was not measurably diminishing the PSC stability. To understand the reproducibility of the PSCs, a statistical distribution of results for 22 reference and 24 RbI devices is shown in Figure 4d,e, Supporting Information and Figure S11c,d, Supporting Information. The distribution of PV parameters showed a significantly smaller spread for the RbI-PSCs compared with the reference, and the average V_{OC} was enhanced by 61 mV. To demonstrate the high V_{OC} potential of the PSCs with addition of RbI, the statistical performance without measurement aperture, i.e., with illumination of the whole active area of the cells, was also included (Figure 4d,e and Figure S11c,d, Supporting Information). An average value of 0.846 V is found. Note, that the active cell area is ill-defined without mask, making the calculation of the current density, thus also PCE, ambiguous for such measurements.

Similar to the aforementioned storage improvement of bare perovskite films measured with PL, the complete PSCs also showed an enhanced performance. During light soaking, as shown in Figure S13a,b, and Table S4, Supporting Information, the reference PSC had a faster light soaking saturation compared with the RbI device, which needed to wait ≈5 min (6 scans) to achieve the best and most stable performance. The V_{OC} of the RbI-containing PSC needed a long light soaking to reach the maximum, gradually increasing during the measurement and reaching 0.823 V, without the FF diminishing concurrently. This effect probably represents the cumulative impact of several phenomena, such as the PL quantum yield increase,[45] ion migration reduction (see below for further discussion),[46] decrease in the density of trap states,[47,48] and photoconductance improvement.[49] A statistical overview of the enhanced performance is shown in Figure S13c–f, Supporting Information. The

J_{SC} and V_{OC} of Sn-Pb PSCs increased significantly after 4 days of storage, especially the V_{OC} of RbI-containing PSCs, which increased to 0.820 V on average. This should be attributed to the recombination reduction demonstrated by the enhanced QFLS. The average FF of RbI-containing PSCs decreased slightly compared with the reference devices, which may be affected by the Rb-Cs accumulation on the perovskite surface. Two other alkali metal salts, CsI and potassium iodide (KI), were also investigated analogously to the RbI study, to check performance improvements in the $FA_{0.83}Cs_{0.17}Pb_{0.5}Sn_{0.5}I_3$ composition. As shown in Figure S14, Supporting Information, only RbI leads to higher V_{OC} in PSCs. In contrast, the V_{OC} and FF of PSCs with CsI and KI additives showed lower values as compared with reference PSCs (Figure 4). This may be due to excess Cs atoms being unbale to embed into Sn-Pb perovskite crystals and instead accumulating on the surface, while K ions are too small to stay in the perovskite crystals in a stable state.

Interestingly, the hysteresis exhibited by Sn-Pb PSCs was reduced after using the RbI additive (Figure 4a). To investigate the mechanism of this effect further, ion migration was characterized by measuring fast hysteresis and current decay, reported previously by some of the authors of this paper.[45,50] As shown in Figure 4f–h, the absolute difference in FF between very fast forward and reverse scan of RbI PSCs was strongly reduced. The peak values for both FF and V_{OC} were found at a much faster scan speed compared to reference devices. In addition, the current loss of RbI-containing PSCs was slightly reduced compared to the reference, where the RbI device had just a 0.88 mA cm^{-2} loss compared with the 2.14 mA cm^{-2} loss of the reference seen for various scanning rates. Moreover, the current density decay in Figure S15, Supporting Information, also demonstrated a shorter decay of RbI-containing PSCs compared with the reference, which was consistent with the "peak hysteresis" observed at faster timescales. As a result, the RbI-containing PSCs had less PCE losses compared to the reference, as shown in Figure 4i. Overall, the RbI additive could boost Sn-Pb PSCs development with higher V_{OC}, smaller current density, and less hysteresis for better PV performance.

3. Conclusions

In this work, the alkali metal salt RbI was employed as an additive for MA-free Sn-Pb perovskites. Following a comprehensive investigation, the working mechanism of the RbI additive, and corresponding changes in interface-related non-radiative recombination losses with and without carrier transport materials were expounded. The composition of perovskite was modified due to the gradient distribution of Rb from the surface to the bulk. Moreover, a carrier lifetime >9 µs was achieved for the RbI-containing Sn-Pb sample. The RbI additive was further found to decrease the density of occupied defects at the perovskite surface by around one order of magnitude. The decreased defect density was found to be correlated with a decrease in the hole carrier concentration by a factor of 72, leading to a more intrinsic perovskite layer. As a result of the lower defect densities, the V_{OC} of RbI-containing PSCs was significantly improved to more than 0.820 V (measured with aperture), i.e., an increase of 61 mV on average. Furthermore, the RbI reduced the hysteresis, and the ion migration as well as current loss of PSCs. Our study has thus established an efficient approach to understanding and addressing the recombination losses of Sn-Pb perovskites. Using the RbI additive presents an efficient path for the development of highly efficient MA-free Sn-Pb PSCs and their application in all-perovskite tandem solar cells.

Supporting Information

Supporting Information is available from the Wiley Online Library or from the author.

Acknowledgements

The authors appreciated the technical assistance from C. Ferber, T. Lußky, H. Heinz, C. Klimm, and J. Beckedahl at the Helmholtz-Zentrum Berlin (HZB). The authors acknowledged funding from the Deutsche Forschungsgemeinschaft (DFG, German Research Foundation) within the SPP 2196 (HIPSTER 424709669). J.T. thanks the Rank Prize fund for financial support. K. P. acknowledged the Deutscher Akademischer Austauschdienst (DAAD) for funding via the Research Grants-Doctoral Programmes in Germany, 2018/19 (57381412). M.S. further acknowledges the Heisenberg program from the DFG for funding, Project No. 498155101. This work was partly funded by EPSRC, project number EP/S004947/1. Additional funding was provided by the Federal Ministry of Education and Research (BMBF) through Young Investigator Group Perovskite Tandem Solar Cells within the program "Materialforschung für die Energiewende" (grant no. 03SF0540) as well as the project PEROWIN (grant no. 03SF0631) and by the Helmholtz Association within the projects HySPRINT Innovation lab, the EU Partnering project TAPAS and the project "Zeitenwende – Tandem Solarzellen". The authors further acknowledge HyPerCells, a joint graduate school of the University of Potsdam and the Helmholtz-Zentrum Berlin. A.M. acknowledges financial support from the German Science Foundation (DFG) in the framework of the priority program SPP 2196 and funding from the European Union HORIZON-MSCA-2021-PF-01-01 under grant agreement no. 101061809 (HyPerGreen). I.L. thanks the AiF project (ZIM-KK5085302DF0) for financial support.

Open access funding enabled and organized by Projekt DEAL.

Conflict of Interest

The authors declare no conflict of interest.

Author Contributions

F.Y. and S.A. coordinated the project and designed the experiments. F.Y. recorded SEM, absolute PL, calculated the QFLS, measured XRD, and analyzed data. D.A. conducted the SEM and EDX mapping, line scan measurement, and analysis. A.A. supported the PL and QFLS measurements with instructions and analysis. F.Y., R.M., and K.P. designed and conducted the trPL characterization, and the data was analyzed by F.Y., R.M., and A.A.. D.M. and L.K. conducted the UPS and XPS measurement and data analysis. A.M. performed the AC Hall measurement and data analysis. J.T., S.S., and M.S. conducted the fast hysteresis measurement and data analysis. I.L. performed the work function characterization by using KP., and supported the coordination of the project. All authors contributed to the data discussion, manuscript writing, and revision. M.S., D.N., H.S., and S.A. supervised the project.

Data Availability Statement

The data that support the findings of this study are available from the corresponding author upon reasonable request.

Keywords

constant final state yield photoelectron spectroscopy, methylammonium-free tin-lead perovskites, quasi-Fermi level splitting, rubidium iodide additive, transient photoluminescence

Received: December 21, 2022
Revised: February 17, 2023
Published online: March 30, 2023

[1] A. Kojima, K. Teshima, Y. Shirai, T. Miyasaka, *J. Am. Chem. Soc.* **2009**, *131*, 6050.
[2] W. Shockley, H. J. Queisser, *J. Appl. Phys.* **1961**, *32*, 510.
[3] D. P. McMeekin, G. Sadoughi, W. Rehman, G. E. Eperon, M. Saliba, M. T. Hörantner, A. Haghighirad, N. Sakai, L. Korte, B. Rech, M. B. Johnston, L. M. Herz, H. J. Snaith, *Science* **2016**, *351*, 151.
[4] Best Research-Cell Efficiencies Chart. National Renewable Energy Laboratory (NREL), Research-Cell-Efficiencies, pdf, 20221207 (accessed: December 2022).
[5] M. A. Green, E. D. Dunlop, J. Hohl-Ebinger, M. Yoshita, N. Kopidakis, K. Bothe, D. Hinken, M. Rauer, X. Hao, **2022**, *29*, 3.
[6] W. Liao, D. Zhao, Y. Yu, N. Shrestha, K. Ghimire, C. R. Grice, C. Wang, Y. Xiao, A. J. Cimaroli, R. J. Ellingson, N. J. Podraza, K. Zhu, R. G. Xiong, Y. Yan, *J. Am. Chem. Soc.* **2016**, *138*, 12360.
[7] F. Hao, C. C. Stoumpos, R. P. H. Chang, M. G. Kanatzidis, *J. Am. Chem. Soc.* **2014**, *136*, 8094.
[8] M. T. Klug, R. L. Milot, R. L. Milot, J. B. Patel, T. Green, H. C. Sansom, M. D. Farrar, A. J. Ramadan, S. Martani, Z. Wang, B. Wenger, J. M. Ball, L. Langshaw, A. Petrozza, M. B. Johnston, L. M. Herz, H. J. Snaith, *Energy Environ. Sci.* **2020**, *13*, 1776.
[9] D. Zhao, C. Chen, C. Wang, M. M. Junda, Z. Song, C. R. Grice, Y. Yu, C. Li, B. Subedi, N. J. Podraza, X. Zhao, G. Fang, R. G. Xiong, K. Zhu, Y. Yan, *Nat. Energy* **2018**, *3*, 1093.
[10] J. Tong, Z. Song, D. H. Kim, X. Chen, C. Chen, A. F. Palmstrom, P. F. Ndione, M. O. Reese, S. P. Dunfield, O. G. Reid, J. Liu, F. Zhang, S. P. Harvey, Z. Li, S. T. Christensen, G. Teeter, D. Zhao, M. M. Al-Jassim, M. F. A. M. Van Hest, M. C. Beard, S. E. Shaheen, J. J. Berry, Y. Yan, K. Zhu, *Science* **2019**, *364*, 475.
[11] R. Lin, K. Xiao, Z. Qin, Q. Han, C. Zhang, M. Wei, M. I. Saidaminov, Y. Gao, J. Xu, M. Xiao, A. Li, J. Zhu, E. H. Sargent, H. Tan, *Nat. Energy* **2019**, *4*, 864.
[12] G. Kapil, T. Bessho, C. H. Ng, K. Hamada, M. Pandey, M. A. Kamarudin, D. Hirotani, T. Kinoshita, T. Minemoto, Q. Shen, T. Toyoda, T. N. Murakami, H. Segawa, S. Hayase, *ACS Energy Lett.* **2019**, *4*, 1991.
[13] K. Xiao, R. Lin, Q. Han, Y. Hou, Z. Qin, H. T. Nguyen, J. Wen, M. Wei, V. Yeddu, M. I. Saidaminov, Y. Gao, X. Luo, Y. Wang, H. Gao, C. Zhang, J. Xu, J. Zhu, E. H. Sargent, H. Tan, *Nat. Energy* **2020**, *5*, 870.
[14] R. Lin, J. Xu, M. Wei, Y. Wang, Z. Qin, Z. Liu, J. Wu, K. Xiao, B. Chen, S. M. Park, G. Chen, H. R. Atapattu, K. R. Graham, J. Xu, J. Zhu, L. Li, C. Zhang, E. H. Sargent, H. Tan, *Nature* **2022**, *603*, 73.
[15] J. Tong, Q. Jiang, A. J. Ferguson, A. F. Palmstrom, X. Wang, J. Hao, S. P. Dunfield, A. E. Louks, S. P. Harvey, C. Li, H. Lu, R. M. France, S. A. Johnson, F. Zhang, M. Yang, J. F. Geisz, M. D. McGehee, M. C. Beard, Y. Yan, D. Kuciauskas, J. J. Berry, K. Zhu, *Nat. Energy* **2022**, *7*, 642.
[16] M. Wei, K. Xiao, G. Walters, R. Lin, Y. Zhao, M. I. Saidaminov, P. Todorović, A. Johnston, Z. Huang, H. Chen, A. Li, J. Zhu, Z. Yang, Y. K. Wang, A. H. Proppe, S. O. Kelley, Y. Hou, O. Voznyy, H. Tan, E. H. Sargent, *Adv. Mater.* **2020**, *32*, 1907058.
[17] G. Kapil, T. Bessho, T. Maekawa, A. K. Baranwal, Y. Zhang, M. A. Kamarudin, D. Hirotani, Q. Shen, H. Segawa, S. Hayase, *Adv. Energy Mater.* **2021**, *11*, 2101069.
[18] S. Hu, K. Otsuka, R. Murdey, T. Nakamura, M. A. Truong, T. Yamada, T. Handa, K. Matsuda, K. Nakano, A. Sato, K. Marumoto, K. Tajima, Y. Kanemitsu, A. Wakamiya, *Energy Environ. Sci.* **2022**, *15*, 2096.
[19] S. R. Sahamir, M. A. Kamarudin, T. S. Ripolles, A. K. Baranwal, G. Kapil, Q. Shen, H. Segawa, J. Bisquert, S. Hayase, *J. Phys. Chem. Lett.* **2022**, *13*, 3130.
[20] S. H. Turren-Cruz, A. Hagfeldt, M. Saliba, *Science* **2018**, *362*, 449.
[21] X. X. Gao, W. Luo, Y. Zhang, R. Hu, B. Zhang, A. Züttel, Y. Feng, M. K. Nazeeruddin, *Adv. Mater.* **2020**, *32*, 1905502.
[22] S. Gharibzadeh, P. Fassl, I. M. Hossain, P. Rohrbeck, M. Frericks, M. Schmidt, T. Duong, M. R. Khan, T. Abzieher, B. A. Nejand, F. Schackmar, O. Almora, T. Feeney, R. Singh, D. Fuchs, U. Lemmer, J. P. Hofmann, S. A. L. Weber, U. W. Paetzold, *Energy Environ. Sci.* **2021**, *14*, 5875.
[23] Y. Zhao, Z. Qu, S. Yu, T. Shen, H. Deng, X. Chu, X. Peng, Y. Yuan, X. Zhang, J. You, **2022**, *534*, 531.
[24] H. Liu, J. Sun, H. Hu, Y. Li, B. Hu, B. Xu, W. C. H. Choy, *ACS Appl. Mater. Interfaces* **2021**, *13*, 45059.
[25] H. Guo, H. Zhang, S. Liu, D. Zhang, Y. Wu, W. H. Zhu, *ACS Appl. Mater. Interfaces* **2022**, *14*, 6852.
[26] T. Jiang, X. Xu, Z. Lan, Z. Chen, X. Chen, T. Liu, S. Huang, Y. (Michael) Yang, *SSRN Electron. J.* **2022**, *101*, 107596.
[27] J. Werner, T. Moot, T. A. Gossett, I. E. Gould, A. F. Palmstrom, E. J. Wolf, C. C. Boyd, M. F. A. M. van Hest, J. M. Luther, J. J. Berry, M. D. McGehee, *ACS Energy Lett.* **2020**, *5*, 1215.
[28] P. Wu, J. Wen, Y. Wang, Z. Liu, R. Lin, H. Li, H. Luo, H. Tan, *Adv. Energy Mater.* **2022**, 2202948.
[29] D. Menzel, A. Tejada, A. Al-Ashouri, I. Levine, J. A. Guerra, B. Rech, S. Albrecht, L. Korte, *ACS Appl. Mater. Interfaces* **2021**, *13*, 43540.
[30] D. Menzel, A. Al-Ashouri, A. Tejada, I. Levine, J. A. Guerra, B. Rech, S. Albrecht, L. Korte, *Adv. Energy Mater.* **2022**, *12*, 2201109.
[31] G. Grancini, S. Marras, M. Prato, C. Giannini, C. Quarti, F. De Angelis, M. De Bastiani, G. E. Eperon, H. J. Snaith, L. Manna, A. Petrozza, *J. Phys. Chem. Lett.* **2014**, *5*, 3836.
[32] F. Yang, J. Liu, X. Wang, K. Tanaka, K. Shinokita, Y. Miyauchi, A. Wakamiya, K. Matsuda, *ACS Appl. Mater. Interfaces* **2019**, *11*, 15680.
[33] G. Zheng, C. Zhu, J. Ma, X. Zhang, G. Tang, R. Li, Y. Chen, L. Li, J. Hu, J. Hong, Q. Chen, X. Gao, H. Zhou, *Nat. Commun.* **2018**, *9*, 1038.
[34] W. Tang, J. Zhang, S. Ratnasingham, F. Liscio, K. Chen, T. Liu, K. Wan, E. S. Galindez, E. Bilotti, M. Reece, M. Baxendale, S. Milita, M. A. McLachlan, L. Su, O. Fenwick, *J. Mater. Chem. A* **2020**, *8*, 13594.
[35] P. Makuła, M. Pacia, W. Macyk, *J. Phys. Chem. Lett.* **2018**, *9*, 6814.
[36] R. T. Ross, *J. Chem. Phys.* **1967**, *46*, 4590.
[37] K. Zhang, K. Forberich, L. Lüer, J. G. Cerrillo, W. Meng, X. Du, V. M. Le Corre, Y. Zhao, T. Niu, Q. Xue, L. J. A. Koster, N. Li, C. J. Brabec, *Adv. Energy Sustainability Res.* **2022**, *3*, 2100156.
[38] A. Al-Ashouri, A. Magomedov, M. Roß, M. Jošt, M. Talaikis, G. Chistiakova, T. Bertram, J. A. Márquez, E. Köhnen, E. Kasparavičius, S. Levcenco, L. Gil-Escrig, C. J. Hages, R. Schlatmann, B. Rech, T. Malinauskas, T. Unold, C. A. Kaufmann, L. Korte, G. Niaura, V. Getautis, S. Albrecht, *Energy Environ. Sci.* **2019**, *12*, 3356.
[39] A. Al-Ashouri, E. Köhnen, B. Li, A. Magomedov, H. Hempel, P. Caprioglio, J. A. Márquez, A. B. M. Vilches, E. Kasparavicius, J. A. Smith, N. Phung, D. Menzel, M. Grischek, L. Kegelmann, D. Skroblin, C. Gollwitzer, T. Malinauskas, M. Jošt, G. Matič, B. Rech, R. Schlatmann, M. Topič, L. Korte, A. Abate, B. Stannowski,

D. Neher, M. Stolterfoht, T. Unold, V. Getautis, S. Albrecht, *Science* **2020**, *370*, 1300.
[40] C. Wang, Y. Zhao, T. Ma, Y. An, R. He, J. Zhu, C. Chen, S. Ren, F. Fu, D. Zhao, X. Li, *Nat. Energy* **2022**, *7*, 744.
[41] H. Kim, J. W. Lee, G. R. Han, Y. J. Kim, S. H. Kim, S. K. Kim, S. K. Kwak, J. H. Oh, *Adv. Funct. Mater.* **2022**, *32*, 2110069.
[42] B. Krogmeier, F. Staub, D. Grabowski, U. Rau, T. Kirchartz, *Sustainability Energy Fuels* **2018**, *2*, 1027.
[43] G. Xu, P. Bi, S. Wang, R. Xue, J. Zhang, H. Chen, W. Chen, X. Hao, Y. Li, Y. Li, *Adv. Funct. Mater.* **2018**, *28*, 1804427.
[44] J. Thiesbrummel, V. M. Le Corre, F. Peña-Camargo, L. Perdigón-Toro, F. Lang, F. Yang, M. Grischek, E. Gutierrez-Partida, J. Warby, M. D. Farrar, S. Mahesh, P. Caprioglio, S. Albrecht, D. Neher, H. J. Snaith, M. Stolterfoht, *Adv. Energy Mater.* **2021**, *11*, 2101447.
[45] S. D. Stranks, V. M. Burlakov, T. Leijtens, J. M. Ball, A. Goriely, H. J. Snaith, *Phys. Rev. Appl.* **2014**, *2*, 034007.
[46] T. Zhang, S. H. Cheung, X. Meng, L. Zhu, Y. Bai, C. H. Y. Ho, S. Xiao, Q. Xue, S. K. So, S. Yang, *J. Phys. Chem. Lett.* **2017**, *8*, 5069.
[47] D. W. DeQuilettes, W. Zhang, V. M. Burlakov, D. J. Graham, T. Leijtens, A. Osherov, V. Bulović, H. J. Snaith, D. S. Ginger, S. D. Stranks, *Nat. Commun.* **2016**, *7*, 11683.
[48] J. S. W. Godding, A. J. Ramadan, Y. H. Lin, K. Schutt, H. J. Snaith, B. Wenger, *Joule* **2019**, *3*, 2716.
[49] D. Guo, Z. Andaji Garmaroudi, M. Abdi-Jalebi, S. D. Stranks, T. J. Savenije, *ACS Energy Lett.* **2019**, *4*, 2360.
[50] V. M. Le Corre, J. Diekmann, F. Peña-Camargo, J. Thiesbrummel, N. Tokmoldin, E. Gutierrez-Partida, K. P. Peters, L. Perdigón-Toro, M. H. Futscher, F. Lang, J. Warby, H. J. Snaith, D. Neher, M. Stolterfoht, *Sol. RRL* **2022**, *6*, 2100772.